Journal of Computational Physics 229 (2010) 4143–4158

Contents lists available at ScienceDirect

Journal of Computational Physics

journal homepage: www.elsevier.com/locate/jcp

A posteriori error estimation and adaptive mesh refinement for a multiscale operator decomposition approach to fluid–solid heat transfer

Donald Estep [a,*], Simon Tavener [b], Tim Wildey [c]

[a] Department of Mathematics and Department of Statistics, Colorado State University, Fort Collins, CO 80523-1874, USA
[b] Department of Mathematics, Colorado State University, Fort Collins, CO 80523-1874, USA
[c] The Institute for Computational Engineering and Sciences, The University of Texas, Austin, TX 78712, USA

ARTICLE INFO

Article history:
Received 28 March 2008
Received in revised form 7 January 2010
Accepted 4 February 2010
Available online 17 February 2010

Keywords:
Adjoint problem
Adaptive mesh refinement
A posteriori error analysis
Boundary flux correction
Conjugate heat transfer
Finite element method
Flux recovery
Greens functions
Operator decomposition
Multi-discretization methods
Multiscale methods

ABSTRACT

We analyze a multiscale operator decomposition finite element method for a conjugate heat transfer problem consisting of a fluid and a solid coupled through a common boundary. We derive accurate *a posteriori* error estimates that account for all sources of error, and in particular the transfer of error between fluid and solid domains. We use these estimates to guide adaptive mesh refinement. In addition, we provide compelling numerical evidence that the order of convergence of the operator decomposition method is limited by the accuracy of the transferred gradient information, and adapt a so-called boundary flux recovery method developed for elliptic problems in order to regain the optimal order of accuracy in an efficient manner. In an appendix, we provide an argument that explains the numerical results provided sufficient smoothness is assumed.

1. Introduction

Multiscale operator decomposition is an attractive approach for computing complex phenomena involving multiple physical processes, multiple scales and/or multiple domains. As such, operator decomposition is ubiquitous in computational science and engineering for multi-physics simulations. The general strategy is to decompose the problem into components involving simpler physics over a relatively limited range of scales, discretize each component using appropriate numerical methods at appropriate scales, and then to seek the solution of the entire system through an iterative procedure involving solutions of the individual components. This approach is appealing because there is a good understanding of how to solve a broad range of single physics problems accurately and efficiently, and because it provides a way to accommodate the multiple scales characteristic of multi-physics problems.

A commonly occurring type of operator decomposition concerns problems in which multiple domains share a common boundary and an iterative procedure is constructed whereby information is exchanged across this boundary at every iteration. Here we consider multiscale operator decomposition for the solution of a conjugate heat transfer problem between

* Corresponding author. Tel.: +1 9704916722; fax: +1 9704912161.
E-mail addresses: estep@math.colostate.edu (D. Estep), tavener@math.colostate.edu (S. Tavener), twildey@ices.utexas.edu (T. Wildey).

0021-9991/$ - see front matter © 2010 Elsevier Inc. All rights reserved.
doi:10.1016/j.jcp.2010.02.003

a heat conducting fluid and a solid. We model the temperature field in the solid using the heat equation and apply the Boussinesq approximation within the fluid. The temperature fields in fluid and solid domains are coupled by imposing continuity of temperature and heat flux across the common boundary. The solid and the fluid may have different thermal conductivities and may be subject to different heat sources and boundary conditions. We allow the possibility that different scales and even different numerical methods may be used to solve for the temperature field in the solid and to solve for the velocity and temperature field in the fluid. Our focus is on the effect of such a multiscale operator decomposition on the accuracy of the solution and on constructing accurate *a posteriori* error estimates which are sensitive to the effects of such decompositions. Adjoint-based *a posteriori* analysis provides a valuable tool for determining how specific terms in a computational approximation generate and propagate error. We consider relatively small Reynolds numbers in order to ensure stable steady solutions and to avoid complications arising from the need to employ numerical stabilization techniques.

The solution of the fully coupled system can be obtained from the multiscale operator decomposition solution in the limit of a (nominally infinite) fixed point iteration during which the current solution in one domain provides boundary conditions for the new solution in the other domain. Adjoint-based variational analysis will be applied to carefully analyze the sources of error. Our goal is to estimate the error in a quantity of interest determined by a functional of the temperature field, and to use this estimate to guide adaptive mesh refinement in order to achieve a user-specified accuracy. We perform an *a posteriori* analysis to obtain error estimates based on the standard techniques using variational analysis, residuals and the adjoint problem [2,8,20,23,18,26]. The standard approach is modified to account for the fact that numerical errors in the solution of each component are propagated to the other component through the boundary conditions, and from one step of the iterative procedure to the next. Both effects are characteristic of operator decomposition and require extensions of the usual *a posteriori* analysis techniques, see [22,19,11,12,29,28].

First, a simplified problem will be presented as a motivational example. We then consider a more sophisticated problem involving the Newtonian flow in a two-dimensional channel past a heated cylinder which is a reasonable, prototypical example of a class of problems commonly solved by operator decomposition. The adjoint analysis clearly identifies a term in the error representation formula corresponding to the transfer of information across the boundary. This term can dominate the error and as we demonstrate, can lead a standard mesh refinement strategy to highly refine near the boundary. We then explain why the "recovered boundary flux" technique developed by Wheeler [33] and Carey [10,9] removes the transfer error and results in significantly different refinement strategies which do not require special refinement near the boundary. Further, numerical results suggest that a straightforward approach to operator decomposition causes a loss in the order of convergence. For our simpler motivational problem, we demonstrate that the "recovered boundary flux" technique provides an inexpensive, nonintrusive way to remedy the loss of order. These examples indicate that an adjoint-based error analysis of operator decomposition methods can not only identify and isolate the mechanisms that generate and propagate the largest errors, but it can also motivate alternative approaches to address the leading sources of error.

In Section 2, we present a model for the flow of a thermally conducting Newtonian fluid past a cylinder and introduce the general iterative multiscale operator decomposition technique. The multiscale operator decomposition finite element method is presented in Section 3. In Section 4 we provide a simple motivational example that illustrates the loss of order of convergence due to operator decomposition. Error estimates are obtained from a detailed *a posteriori* error analysis in Section 5 and used to construct an adaptive mesh refinement strategy. We describe the recovered boundary flux method in Section 6 and its effect on transfer and projection errors. We then reconsider the motivational example of Section 4 and demonstrate the effect of the recovered boundary flux method on convergence rate. The main numerical results for our prototypical example of operator decomposition is addressed in Section 7. Our conclusions are presented in Section 8.

For elliptic problems, it is possible to carry out a rigorous analysis showing that boundary flux method recovers optimal convergence in the L^2 norm [22]. In Appendix A, we briefly describe how this analysis can be extended to the coupled fluid–solid system, provided sufficient smoothness is assumed. The motivation for such a result is that we wish to verify that the *a posteriori* estimate is sensitive to the positive effects of flux recovery and hence avoids calling for unnecessary mesh refinement.

2. Description of flow of a thermally conducting fluid past a cylinder

We consider the steady flow of a heat conducting Newtonian fluid past a solid cylinder as shown in Fig. 1.

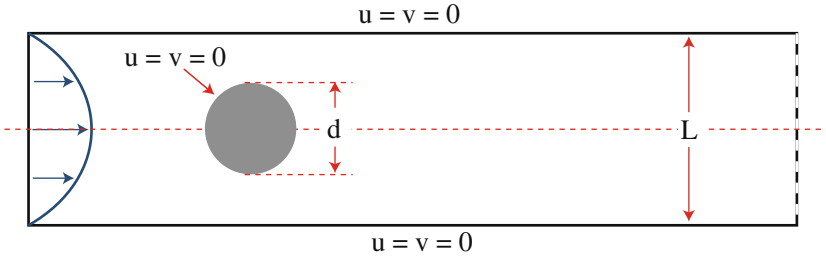

Fig. 1. Computational domain for flow past a cylinder.

We solve the heat equation in the solid and the equations governing the conservation of momentum, mass and energy in the fluid, where we apply the Boussinesq approximation. The temperature field is advected by the fluid and couples back to the momentum equations through the buoyancy term. The goal of the approximate solution is to compute a specified quantity of interest accurately.

2.1. The conjugate heat transfer problem

Let Ω_S and Ω_F be polygonal domains in $\mathbb{R}^2$ with boundaries $\partial\Omega_S$ and $\partial\Omega_F$ intersecting along an interface $\Gamma_I = \partial\Omega_S \cap \partial\Omega_F$. The complete coupled problem is

$$\begin{cases} -\mu\Delta\boldsymbol{u} + \rho_0(\boldsymbol{u}\cdot\nabla)\boldsymbol{u} + \nabla p + \rho_0\beta T_F\mathbf{g} = \rho_0(1+\beta T_0)\mathbf{g}, & x\in\Omega_F,\\ -\nabla\cdot\boldsymbol{u} = 0, & x\in\Omega_F,\\ -k_F\Delta T_F + \rho_0 c_p(\boldsymbol{u}\cdot\nabla T_F) = Q_F, & x\in\Omega_F,\\ \begin{cases} T_S = T_F,\\ k_F(\boldsymbol{n}\cdot\nabla T_F) = k_S(\boldsymbol{n}\cdot\nabla T_S), \end{cases} & x\in\Gamma_I,\\ -k_S\Delta T_S = Q_S, & x\in\Omega_S, \end{cases} \tag{1}$$

where ρ_0 and T_0 are reference values for the density and temperature, respectively, μ is the molecular viscosity, β is the coefficient of thermal expansion, c_p is the specific heat, k_F and k_S are the thermal conductivities of the fluid and solid, respectively, Q_F and Q_S are source terms and $\boldsymbol{n}$ is the unit normal vector directed into the fluid.

We define $\Gamma_{\boldsymbol{u},D}$ and $\Gamma_{\boldsymbol{u},N}$ to be the boundaries on which we apply Dirichlet and Neumann conditions for the velocity field, respectively, and set

$$\begin{cases} \boldsymbol{u} = \mathbf{g}_{\boldsymbol{u},D}, & x\in\Gamma_{\boldsymbol{u},D},\\ \mu\partial\boldsymbol{u}/\partial\boldsymbol{n} = \mathbf{g}_{\boldsymbol{u},N}, & x\in\Gamma_{\boldsymbol{u},N}. \end{cases}$$

Similarly, we define $\Gamma_{T_F,D}$, $\Gamma_{T_F,N}$, $\Gamma_{T_S,D}$ and $\Gamma_{T_S,N}$ to be the boundaries on which we impose Dirichlet and Neumann conditions for the temperature fields in the fluid and the solid, respectively, and set

$$\begin{cases} T_F = g_{T_F,D}, & x\in\Gamma_{T_F,D},\\ k_F(\boldsymbol{n}\cdot\nabla T_F) = g_{T_F,N}, & x\in\Gamma_{T_F,N},\\ T_S = g_{T_S,D}, & x\in\Gamma_{T_S,D},\\ k_S(\boldsymbol{n}\cdot\nabla T_S) = g_{T_S,N}, & x\in\Gamma_{T_S,N}. \end{cases}$$

To simplify the discussion, we assume that these boundary conditions can be interpolated exactly in the finite element space.

2.2. An iterative operator decomposition problem

Instead of approximating the solution of the fully coupled system (1) directly, we solve an "analytic" operator decomposition problem. Assuming that we have an initial guess, $T_F^{\{0\}}$, for the Dirichlet data along Γ_I, we solve the iterative problem presented in Algorithm 1.

Algorithm 1. Iterative Operator Decomposition Problem

k = 0

while $(\|T_S^{\{k\}} - \pi_S T_F^{\{k\}}\|_{\Gamma_I} > TOL)$ **do**

(a) k = k+1

(b) Given $T_F^{\{k-1\}}$ on Γ_I, compute $T_S^{\{k\}} \in \Omega_S$ by solving

$$\begin{cases} -k_S\Delta T_S^{\{k\}} = Q_S, & x\in\Omega_S\\ T_S^{\{k\}} = T_F^{\{k-1\}}, & x\in\Gamma_I, \end{cases} \tag{2}$$

and boundary conditions on $\Gamma_{T_S,D}$, $\Gamma_{T_S,N}$.

(c) Given $T_S^{\{k\}}$, compute $\boldsymbol{u}^{\{k\}}, p^{\{k\}}, T_F^{\{k\}} \in \Omega_F$ by solving

$$\begin{cases} -\mu\Delta\boldsymbol{u}^{\{k\}} + \rho_0(\boldsymbol{u}^{\{k\}}\cdot\nabla)\boldsymbol{u}^{\{k\}} + \nabla p^{\{k\}} + \rho_0\beta T_F^{\{k\}}\mathbf{g} = \boldsymbol{f}, & x\in\Omega_F\\ -\nabla\cdot\boldsymbol{u}^{\{k\}} = 0, & x\in\Omega_F\\ -k_F\Delta T_F^{\{k\}} + \rho_0 c_p(\boldsymbol{u}^{\{k\}}\cdot\nabla T_F^{\{k\}}) = Q_F, & x\in\Omega_F\\ k_F(\boldsymbol{n}\cdot\nabla T_F^{\{k\}}) = k_S(\boldsymbol{n}\cdot\nabla T_S^{\{k\}}), & x\in\Gamma_I. \end{cases} \tag{3}$$

and boundary conditions on $\Gamma_{\boldsymbol{u},D}$, $\Gamma_{\boldsymbol{u},N}$, $\Gamma_{T_F,D}$ and $\Gamma_{T_F,N}$.

end while

Assuming that the iteration converges, we obtain the solution of the global problem (1) in the limit of an infinite number of iterations. If we end the iteration after a finite number of steps, then there is a difference between the solutions of the global and operator decomposition iteration problem, even without introducing numerical solution error. Hence, an accurate *a posteriori* error analysis must take into account the errors introduced by numerical solution of the component problems (2) and (3) and the effects of finite iteration. Further, when we introduce numerical methods, we will see additional sources of error arising from the "transfer" of information between the component problems.

The iterative operator decomposition problem Algorithm 1 is relatively simple, and there are many other possible versions. This simple iterative scheme may not converge for a particular model problem. In general, the convergence depends on the values of k_S and k_F along the interface and the geometry of each region [24,31,35,22]. As an alternative, we can extend the analysis to a simple relaxation scheme: We choose $\alpha \in [0,1)$ and update the Dirichlet interface values with

$$T_F^{\{k\}} = \alpha T_F^{\{k-1\}} + (1-\alpha) T_S^{\{k-1\}}. \tag{4}$$

By reformulating the fixed point iteration as a root finding problem, other iterative solutions techniques such as preconditioned Newton–Krylov methods [36,21] may also be used to solve operator decomposition problems.

3. The finite element discretization

We begin with the weak formulation of the global problem (1) in order to introduce notation and various spaces.

3.1. Weak formulation of the global problem

Let $L^2(\Omega)$ denote the space of square integrable functions on Ω with inner product $(\cdot,\cdot)_\Omega$ and norm $\|\cdot\|_\Omega$, or simply $(\cdot,\cdot)$ when the domain is clear. We use $H^s(\Omega)$ to denote the Sobolev space with real index s associated with the norm $\|\cdot\|_{\Omega,s}$ and seminorm $|\cdot|_{\Omega,s}$ [1,6] with the obvious generalization to vector valued functions.

The weak formulation of (1) seeks $\boldsymbol{u} \in \mathbf{V}_F,\ p \in L_0^2(\Omega_F),\ T_F \in W_F$ and $T_S \in W_S$ such that $T_F = T_S$ on Γ_I and

$$\begin{cases} a_1(\boldsymbol{u},\boldsymbol{v}) + c_1(\boldsymbol{u},\boldsymbol{u},\boldsymbol{v}) + b(\boldsymbol{v},p) + d(T_F,\boldsymbol{v}) = (\boldsymbol{f},\boldsymbol{v}), \\ b(\boldsymbol{u},q) = 0, \\ a_2(T_F,w_F) + c_2(\boldsymbol{u},T_F,w_F) + a_3(T_S,w_S) = (Q_F,w_F) + (Q_S,w_S), \end{cases} \tag{5}$$

for all $\boldsymbol{v} \in \boldsymbol{V}_{F,0},\ q \in L_0^2(\Omega_F),\ w_F \in W_{F,0}$ and $w_S \in W_{S,0}$ with $w_F = w_S$ on Γ_I, where

$$\begin{aligned} a_1(\boldsymbol{u},\boldsymbol{v}) &= \int_{\Omega_F} \mu(\nabla \boldsymbol{u} : \nabla \boldsymbol{v})dx, \quad a_2(T_F,w_F) = \int_{\Omega_F} k_F(\nabla T_F \cdot \nabla w_F)dx, \\ a_3(T_S,w_S) &= \int_{\Omega_S} k_S(\nabla T_S \cdot \nabla w_S)dx, \quad b(\boldsymbol{v},q) = -\int_{\Omega_F} (\nabla \cdot \boldsymbol{v}) q\,dx, \\ c_1(\boldsymbol{u},\boldsymbol{v},\boldsymbol{z}) &= \int_{\Omega_F} \rho_0(\boldsymbol{u}\cdot\nabla)\boldsymbol{v}\cdot\boldsymbol{z}\,dx, \quad c_2(\boldsymbol{u},T,w) = \int_{\Omega_F} \rho_0 c_p(\boldsymbol{u}\cdot\nabla T) w\,dx, \\ d(T,\boldsymbol{v}) &= \int_{\Omega_F} \rho_0 \beta T \mathbf{g}\cdot\boldsymbol{v}\,dx, \quad \boldsymbol{f} = \rho_0(1+\beta T_0)\mathbf{g}. \end{aligned}$$

Here

$$\begin{aligned} \boldsymbol{V}_F &= \{\boldsymbol{v} \in \mathbf{H}^1(\Omega_F) | \boldsymbol{v} = \boldsymbol{g}_{\boldsymbol{u},D} \text{ on } \Gamma_{\boldsymbol{u},D}\}, \quad \boldsymbol{V}_{F,0} = \{\boldsymbol{v} \in \boldsymbol{V}_F | \boldsymbol{v} = \mathbf{0} \text{ on } \Gamma_{\boldsymbol{u},D}\}, \\ W_F &= \{w \in H^1(\Omega_F) | w = g_{T_F,D} \text{ on } \Gamma_{T_F,D}\}, \quad W_{F,0} = \{w \in W_F | w = 0 \text{ on } \Gamma_{T_F,D}\}, \\ W_S &= \{w \in H^1(\Omega_S) | w = g_{T_S,D} \text{ on } \Gamma_{T_S,D}\}, \quad W_{S,0} = \{w \in W_S | w = 0 \text{ on } \Gamma_{T_S,D}\}, \end{aligned}$$

and

$$L_0^2(\Omega) = \left\{ v \in L^2(\Omega) \middle| \int_\Omega v\,dx = 0 \right\},$$

and in particular,

$$Z = L_0^2(\Omega_F).$$

The continuity of thermal flux across the interface Γ_I is satisfied in the 3rd (and final) equation of (5) as can be seen by integration by parts. We assume that the source terms and the boundary data are sufficiently small and the molecular viscosity μ and thermal conductivities k_F and k_S are sufficiently large so that (5) admits a regular weak solution.

3.2. Finite element discretization of the operator decomposition problem

Let $\mathcal{T}_{F,h}$ and $\mathcal{T}_{S,h}$ be locally quasi-uniform triangulations of Ω_F and Ω_S, respectively. We do not assume that the triangulations on either side of Γ_I are aligned.

We use the piecewise polynomial spaces

$$\boldsymbol{V}_F^h = \left\{\mathbf{v} \in \boldsymbol{V}_F | \boldsymbol{v} \text{ continuous on } \Omega_F,\ \boldsymbol{v_i} \in \boldsymbol{P}^2(\boldsymbol{K}) \text{ for all } \boldsymbol{K} \in \mathcal{T}_{F,h}\right\},$$
$$Z^h = \left\{z \in Z | z \text{ continuous on } \Omega_F,\ z \in P^1(K) \text{ for all } K \in \mathcal{T}_{F,h}\right\},$$
$$W_F^h = \left\{w \in W_F | w \text{ continuous on } \Omega_F,\ w \in P^2(K) \text{ for all } K \in \mathcal{T}_{F,h}\right\},$$
$$W_S^h = \left\{w \in W_S | w \text{ continuous on } \Omega_S,\ w \in P^2(K) \text{ for all } K \in \mathcal{T}_{S,h}\right\},$$

and the associated subspaces

$$\boldsymbol{V}_{F,0}^h = \left\{\boldsymbol{v} \in \boldsymbol{V}^h | \boldsymbol{v} = 0 \text{ on } \Gamma_{\boldsymbol{u},D}\right\},$$
$$W_{F,0}^h = \left\{w \in W_F^h | w = 0 \text{ on } \Gamma_{T_F,D}\right\},$$
$$W_{S,0}^h = \left\{w \in W_S^h | w = 0 \text{ on } \Gamma_{T_S,D} \text{ and } w = 0 \text{ on } \Gamma_I\right\},$$

where $P^q(K)$ denotes the space of polynomials of degree q on an element K. Note that functions in $W_{S,0}^h$ are required to be zero on Γ_I, while functions in $W_{F,0}^h$ are not required to vanish on the interface between the fluid and solid. We let $\pi_{\boldsymbol{V}},\ \pi_{W_F},\ \pi_{W_S}$ and π_Z be projections into $\boldsymbol{V}_F^h, W_F^h,\ W_S^h$ and Z^h, respectively, and also use π_{W_F} and π_{W_S} to denote projections into W_F^h and W_S^h, respectively along the interface Γ_I. Projecting information between discretizations is a non-trivial matter, especially in three dimensions or if the discretized representations of the geometry are not the same. For simplicity, we assume that the geometric representation of the interface between the solid and the fluid is the same for each discretization as shown in Fig. 2. We have chosen V_F^h and Z^h to be the Taylor–Hood finite element pair which is known to satisfy the discrete *inf–sup* condition

$$\inf_{q \in Z^h} \sup_{\boldsymbol{v} \in \boldsymbol{V}_F^h} \frac{b(\boldsymbol{v}, q)}{\|\boldsymbol{v}\|_1 \cdot \|q\|_0} \geqslant \beta > 0. \tag{6}$$

The multiscale Operator Decomposition Finite Element Method corresponding to Algorithm 1 is provided in Algorithm 2.

Algorithm 2. Multiscale Operator Decomposition Finite Element Method: OD-FEM

k = 0

while $(\|T_S^{\{k\}} - \pi_S T_F^{\{k\}}\|_{\Gamma_I} > TOL)$ **do**

(a) k = k+1

Find $T_{S,h}^{\{k\}} \in W_S^h$ such that $T_{S,h}^{\{k\}} = \pi_{W_S} T_{F,h}^{\{k-1\}}$ along the interface Γ_I and

$$a_3(T_{S,h}^{\{k\}}, w) = (Q_S, w), \quad \text{for all } w \in W_{S,0}^h, \tag{7}$$

(c) Find $\boldsymbol{u}_h^{\{k\}} \in \boldsymbol{V}_F^h,\ p_h^{\{k\}} \in Z^h$ and $T_{F,h}^{\{k\}} \in W_F^h$ such that

$$\begin{cases} a_1(\boldsymbol{u}_h^{\{k\}}, \boldsymbol{v}) + c_1(\boldsymbol{u}_h^{\{k\}}, \boldsymbol{u}_h^{\{k\}}, \boldsymbol{v}) + b(\boldsymbol{v}, p_h^{\{k\}}) + d(T_{F,h}^{\{k\}}, \boldsymbol{v}) = (\boldsymbol{f}, \boldsymbol{v}), \\ b(\boldsymbol{u}_h^{\{k\}}, q) = 0, \\ a_2(T_{F,h}^{\{k\}}, w) + c_2(\boldsymbol{u}_h^{\{k\}}, T_{F,h}^{\{k\}}, w) = (Q_F, w) - (\chi^{\{k\}}, w)_{\Gamma_I}, \end{cases} \tag{8}$$

for all $\boldsymbol{v} \in \boldsymbol{V}_{F,0}^h,\ q \in Z^h,\ w \in W_{F,0}^h$ and $\chi^{\{k\}} = k_S(\boldsymbol{n} \cdot \nabla T_{S,h}^{\{k\}})$.

end while

4. Motivational example illustrating loss of order

We apply Algorithm 2 to the steady flow of a Newtonian fluid in a two-dimensional domain connected along one boundary to a solid which is heated from below as shown in Fig. 3.

The temperature is defined to be 1 along $y = 0$ and 0 along $y = 3$ with adiabatic boundary conditions on the remaining outer boundaries. Continuity of temperature and normal heat flux are imposed at the interface. We set $\boldsymbol{u} \cdot \boldsymbol{n} = 0$ along the fluid boundaries. The thermal conductivities are $k_F = 1$ and $k_S = \exp(1 + 0.5\sin(\pi x))$, which are chosen to give a smooth solution. The x-dependence of the thermal conductivity in the solid ensures that the interface between the solid and the fluid is not an isothermal surface. This in turn implies that for any values of the temperature gradient there is not a "conducting" solution (non-convecting solution) for which the velocity field is identically zero and the buoyancy force is exactly balanced by a vertical gradient in the pressure field. The (non-zero) velocity fields are given in Fig. 4.

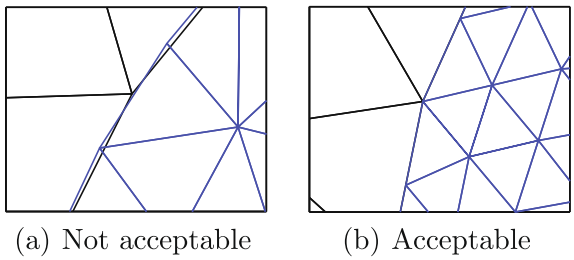

Fig. 2. Two examples of the geometric representation of the fluid–solid interface.

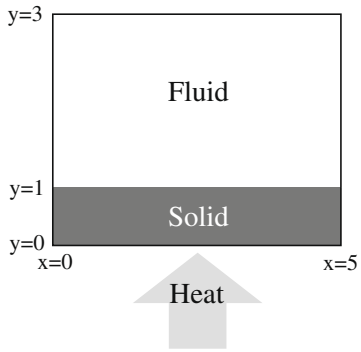

Fig. 3. Computational domain for motivational example.

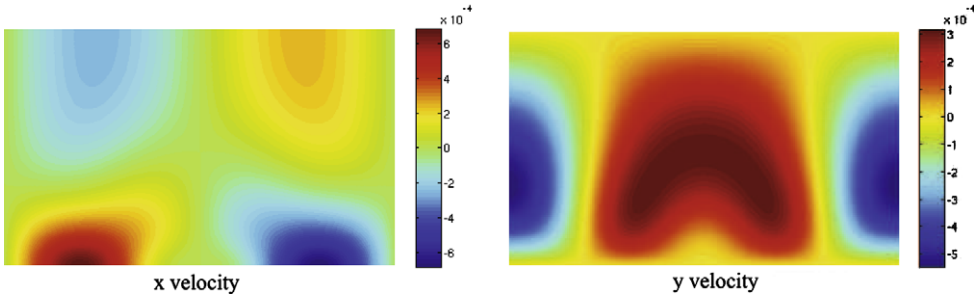

Fig. 4. Fluid velocities for the motivational example.

We solve the problem iteratively using $\chi^{\{k\}} = k_S(\boldsymbol{n} \cdot \nabla T_{S,h}^{\{k\}})$ in Eq. (8) and compute a reference solution with a higher order method on the same mesh. In Table 1, we compare the L^2 errors in the velocity, pressure and temperature fields on a series of uniform meshes that align along the interface Γ_I.

We observe that the pressure field converges at the optimal quadratic rate. However, the velocities and the temperature fields converge at a suboptimal quadratic rate, rather than at the expected cubic rate. This loss of order is a consequence of the operator decomposition. The computed boundary flux obtained from the finite element solution is one order less accurate than the solution itself and this error pollutes the rest of the computation.

This loss of order is a general phenomena affecting finite element solutions of coupled problems that include passing of flux information across a boundary. There are some simple situations in which the flux values can be represented exactly in the finite element space, but this is fairly rare. Given the many sources of error in such computations, the loss of order of convergence may be observed only for fairly refined discretizations [22].

5. *A posteriori* error analysis of OD-FEM

To estimate the error of the multi-discretization operator decomposition finite element approximation, we apply *a posteriori* techniques based on variational analysis and the adjoint problem. We begin by discussing one possible formulation of

Table 1
Mesh sizes, number of elements, and L^2 errors for the motivational example using the finite element flux.

h	NELEM	Fluid temperature	Solid temperature	x-Velocity	y-Velocity	Pressure
1/2	120	2.22E−3	1.67E−3	2.02E−4	2.47E−4	2.39E−1
1/4	480	7.54E−4	5.24E−4	5.80E−5	5.67E−5	7.99E−2
1/8	1920	1.25E−4	9.70E−5	2.20E−5	1.38E−5	1.83E−2
Conv. Rates		2.07	2.05	1.60	2.08	1.85

an adjoint problem for the Boussinesq equations. Since these are nonlinear, there is not a unique adjoint problem. The adjoint problem for the heat equation component follows standard definitions.

5.1. The adjoint to the Boussinesq equations

Defining the adjoint to the Boussinesq operator,

$$\boldsymbol{B}(\boldsymbol{u},p,T)=\begin{pmatrix}\mu\Delta\boldsymbol{u}+\rho_0(\boldsymbol{u}\cdot\nabla)\boldsymbol{u}+\nabla p+\rho_0\beta T_F\mathbf{g}\\ -\nabla\cdot\boldsymbol{u}\\ -k_F\Delta T_F+\rho_0 c_p(\boldsymbol{u}\cdot\nabla T_F)\end{pmatrix},$$

is complicated by the fact that it is nonlinear. In general, there is not a unique adjoint associated with a nonlinear operator. However, we can use linearization to define an adjoint for the purposes of error analysis. Let $\boldsymbol{u}_h$, p_h and T_h be approximation to $\boldsymbol{u}$, p and T, respectively and define

$$\boldsymbol{e}=(\boldsymbol{u}-\boldsymbol{u}_h,p-p_h,T-T_h).$$

Formally, we define the linearized adjoint operator, $\overline{\boldsymbol{B}}^*$, such that

$$(\boldsymbol{B}(\boldsymbol{u},p,T),\boldsymbol{\phi})-(\boldsymbol{B}(\boldsymbol{u}_h,p_h,T_h),\boldsymbol{\phi})=\big(\overline{\boldsymbol{B}}(\boldsymbol{e}),\boldsymbol{\phi}\big)=\big(\boldsymbol{e},\overline{\boldsymbol{B}}^*(\boldsymbol{\phi})\big),$$

where the linearized operator, $\overline{\boldsymbol{B}}$, is defined by

$$\overline{\boldsymbol{B}}(\boldsymbol{e})=\int_0^1\boldsymbol{B}'(s\boldsymbol{u}+(1-s)\boldsymbol{u}_h,sp+(1-s)p_h,sT+(1-s)T_h)\boldsymbol{e}\,ds$$

where

$$\boldsymbol{B}'(\boldsymbol{u},p,T)=\left(\frac{\partial\boldsymbol{B}}{\partial\boldsymbol{u}}(\boldsymbol{u},p,T)\ \frac{\partial\boldsymbol{B}}{\partial p}(\boldsymbol{u},p,T)\ \frac{\partial\boldsymbol{B}}{\partial T}(\boldsymbol{u},p,T)\right)^{\top}.$$

We write the formal adjoint to the Boussinesq equations in strong form as

$$\begin{cases}-\mu\Delta\boldsymbol{\phi}+\overline{\mathbf{c}}_1^*(\boldsymbol{\phi})+\nabla z+\overline{\mathbf{c}}_{2u}^*(\theta)=\boldsymbol{\psi}_{\boldsymbol{u}}, & x\in\Omega,\\ -\nabla\cdot\boldsymbol{\phi}=\psi_p, & x\in\Omega,\\ -k_F\Delta\theta+\overline{c}_{2T}^*(\theta)+\rho_0\beta(\mathbf{g}\cdot\boldsymbol{\phi})=\psi_T, & x\in\Omega,\end{cases}\tag{9}$$

with the adjoint boundary conditions

$$\begin{cases}\boldsymbol{\phi}=\mathbf{0}, & x\in\Gamma_{\boldsymbol{u},D},\\ \mu\partial\boldsymbol{\phi}/\partial\mathbf{n}=\mathbf{0}, & x\in\Gamma_{\boldsymbol{u},N},\\ \theta=0, & x\in\Gamma_{T_F,D}\\ k_F(\mathbf{n}\cdot\nabla\theta)=0, & x\in\Gamma_{T_F,N},\end{cases}\tag{10}$$

where

$$\overline{\mathbf{c}}_1^*(\boldsymbol{\phi})=\rho_0\left(\frac{1}{2}(\nabla\boldsymbol{u})^T+\frac{1}{2}(\nabla\boldsymbol{u}_h)^T\right)\cdot\boldsymbol{\phi}-\rho_0\left(\frac{1}{2}\boldsymbol{u}+\frac{1}{2}\boldsymbol{u}_h\right)\cdot\nabla\boldsymbol{\phi}-\rho_0\left(\nabla\cdot\left(\frac{1}{2}\boldsymbol{u}+\frac{1}{2}\boldsymbol{u}_h\right)\right)\boldsymbol{\phi},$$

$$\overline{\mathbf{c}}_{2u}^*(\theta)=\rho_0 c_p\nabla\left(\frac{1}{2}T+\frac{1}{2}T_h\right)\theta,$$

$$\overline{c}_{2T}^*(\theta)=-\rho_0 c_p\left(\frac{1}{2}\boldsymbol{u}+\frac{1}{2}\boldsymbol{u}_h\right)\cdot\nabla\theta-\rho_0 c_p\left(\nabla\cdot\left(\frac{1}{2}\boldsymbol{u}+\frac{1}{2}\boldsymbol{u}_h\right)\right)\theta.$$

The terms $\boldsymbol{\psi}_{\boldsymbol{u}}$, ψ_p and ψ_T on the right hand side of the adjoint to the Boussinesq operator (9) are chosen based on the linear functional of the error in which we are interested. For example, if we are interested in a linear functional of the error based on the velocity field only, then we define $\boldsymbol{\psi}_{\boldsymbol{u}}$ according to this linear functional and set $\psi_p=\psi_T=0$. Similarly, if we are interested in the error in the temperature field alone, then we set ψ_T as appropriate and $\boldsymbol{\psi}_{\boldsymbol{u}}=\boldsymbol{0}$, $\psi_p=0$.

Remark 5.1. In practice we cannot use the true adjoint (9) since the exact solution is unknown. We therefore linearize the nonlinear operator around the approximate solutions and compute

$$\begin{cases} -\mu\Delta\boldsymbol{\phi} - \rho_0\boldsymbol{u}_h\cdot\nabla\boldsymbol{\phi} + \rho_0\Big((\nabla\boldsymbol{u}_h)^T\cdot\boldsymbol{\phi} - (\nabla\cdot\boldsymbol{u}_h)\boldsymbol{\phi}\Big) + \nabla z + (\rho_0 c_p\nabla T_h)\theta = \boldsymbol{\psi}_{\boldsymbol{u}}, \\ -\nabla\cdot\phi = \psi_p, \\ -k_F\Delta\theta - \rho_0 c_p\boldsymbol{u}_h\cdot\nabla\theta - \rho_0 c_p(\nabla\cdot\boldsymbol{u}_h)\theta + \rho_0\beta(\mathbf{g}\cdot\boldsymbol{\phi}) = \psi_T, \end{cases} \tag{11}$$

with the same adjoint boundary conditions.

The difference between the solution of (9) and the solution of (11) can be viewed as a higher order expression in the error [3,2].

5.2. The adjoint to the conjugate heat transfer problem

We define

$$\boldsymbol{e}_u = \boldsymbol{u} - \boldsymbol{u}_h^{\{k\}}, \quad e_p = p - p_h^{\{k\}}, \quad e_{T_F} = T_F - T_{F,h}^{\{k\}} \quad \text{and} \quad e_{T_S} = T_S - T_{S,h}^{\{k\}}.$$

The adjoint boundary value problem for the quantity of interest

$$(\boldsymbol{\psi},\boldsymbol{e}) = (\boldsymbol{\psi}_{\boldsymbol{u}},\boldsymbol{e}_{\boldsymbol{u}})_{\Omega_F} + (\psi_p,e_p)_{\Omega_F} + (\psi_{T_F},e_{T_F})_{\Omega_F} + (\psi_{T_S},e_{T_S})_{\Omega_S}$$

for the coupled problem (1) is

$$\begin{cases} -\mu\Delta\boldsymbol{\phi} + \overline{\mathbf{c}}_1^*(\boldsymbol{\phi}) + \nabla z + \overline{\mathbf{c}}_{2u}^*(\theta_F) = \boldsymbol{\psi}_{\boldsymbol{u}}, & x\in\Omega_F, \\ -\nabla\cdot\boldsymbol{\phi} = \psi_p, & x\in\Omega_F, \\ -k_F\Delta\theta_F + \overline{c}_{2T}^*(\theta_F) + \rho_0\beta(\mathbf{g}\cdot\boldsymbol{\phi}) = \psi_{T_F}, & x\in\Omega_F, \\ \begin{cases}\theta_F = \theta_S, \\ k_F(\boldsymbol{n}\cdot\nabla\theta_F) = k_S(\boldsymbol{n}\cdot\nabla\theta_S),\end{cases} & x\in\Gamma_I, \\ -k_S\Delta\theta_S = \psi_{T_S}, & x\in\Omega_S, \end{cases} \tag{12}$$

with adjoint boundary conditions

$$\begin{cases} \boldsymbol{\phi} = \mathbf{0}, & x\in\Gamma_{\boldsymbol{u},D}, \\ \mu\frac{\partial\boldsymbol{\phi}}{\partial\boldsymbol{n}} = \mathbf{0}, & x\in\Gamma_{\boldsymbol{u},N}, \\ \theta_F = 0, & x\in\Gamma_{T_F,D}, \\ k_F(\boldsymbol{n}\cdot\nabla\theta_F) = 0, & x\in\Gamma_{T_F,N}, \\ \theta_S = 0, & x\in\Gamma_{T_S,D}, \\ k_S(\boldsymbol{n}\cdot\nabla\theta_S) = 0, & x\in\Gamma_{T_S,N}. \end{cases} \tag{13}$$

We solve (12) numerically using the approximate Boussinesq adjoint (11) and an iterative operator decomposition approach as for the forward problem. These iterations are completely independent of the forward iterations. We note that the adjoint problem is a new differential equation with its own numerical solution requirements. In particular, we want to compute the interpolation error $\boldsymbol{\phi} - \Pi_h\boldsymbol{\phi}$ arising from Galerkin orthogonality which requires solving the adjoint system (12) with a higher order finite element method. Since the adjoint problem is linear, the cost in solving the adjoint problem is approximately the same as taking one Newton step of the forward problem with a higher order method using the previously computed lower order solution as an initial guess. Solving the adjoint problem provides an accurate quantification of the effects of stability on error as we show in Section 5.3.

5.3. An error representation for the iterative procedure

We derive an error representation formula (15) that holds for the basic scheme (2), (3), the weighted relaxation technique (4), and when using the post-processed flux (21). In the discussion below, we use $\chi_h^{\{k\}}$ to denote the value of the normal flux passed at the kth iteration from Ω_S to Ω_F.

To begin, we multiply the system (12) by $\boldsymbol{e}$ and apply the divergence theorem, noting that $\theta_F = \theta_S$ and $k_F(\boldsymbol{n}\cdot\nabla\theta_F) = k_S(\boldsymbol{n}\cdot\nabla\theta_S)$ along Γ_I, to obtain

$$\begin{aligned}(\boldsymbol{\psi},\boldsymbol{e}) = {} & a_1(\boldsymbol{e}_{\boldsymbol{u}},\boldsymbol{\phi}) + c_1(\boldsymbol{u},\boldsymbol{u},\boldsymbol{\phi}) - c_1(\boldsymbol{u}_h^{\{k\}},\boldsymbol{u}_h^{\{k\}},\boldsymbol{\phi}) + b(\boldsymbol{\phi},e_p) + d(e_{T_F},\boldsymbol{\phi}) + b(\boldsymbol{e}_{\boldsymbol{u}},z) + a_2(e_{T_F},\theta_F) + c_2(\boldsymbol{u},T_F,\theta_F) \\ & - c_2(\boldsymbol{u}_h^{\{k\}},T_{F,h}^{\{k\}},\theta_F) + a_3(e_{T_S},\theta_S) + \Big(T_{S,h}^{\{k\}},k_S(\boldsymbol{n}\cdot\nabla\theta_S)\Big)_{\Gamma_I} - \Big(T_{F,h}^{\{k\}},k_F(\boldsymbol{n}\cdot\nabla\theta_F)\Big)_{\Gamma_I}.\end{aligned}$$

Observe that the test space $W_{S,0}^h$ consists of functions that are zero along the interface, while in general, θ_S is not zero along Γ_I. This means that the projection of θ_S into $W_{S,0}^h$ cannot be the interpolant. We define a new projection $\pi_{W_S}^0 : H^2 \to W_{S,0}^h$ such that for any node x_i

$$\pi^0_{W_S}\theta_S(x_i) = \begin{cases} \pi_{W_S}\theta_S(x_i), & x_i \notin \Gamma_I, \\ 0, & x_i \in \Gamma_I. \end{cases} \tag{14}$$

Using the projection (14) in the Galerkin orthogonality relation, we have

$$\begin{aligned}(\psi,\mathbf{e}) &= (\mathbf{f},\phi-\pi_V\phi) - a_1(\mathbf{u}_h^{\{k\}},\phi-\pi_V\phi_1) - c_1(\mathbf{u}_h^{\{k\}},\mathbf{u}_h^{\{k\}},\phi-\pi_V\phi) - b(\phi-\pi_V\phi,p_h) - d(T_{F,h}^{\{k\}},\phi-\pi_V\phi) - b(\mathbf{u}_h^{\{k\}},z-\pi_Z z)\\ &\quad + \left(Q_F,\theta_F-\pi_{W_F}\theta_F\right) - a_2(T_{F,h}^{\{k\}},\theta_F-\pi_{W_F}\theta_F) - c_2(\mathbf{u}_h^{\{k\}},T_{F,h}^{\{k\}},\theta_F-\pi_{W_F}\theta_F) + \left(Q_S,\theta_S-\pi^0_{W_S}\theta_S\right) - a_3(T_{S,h}^{\{k\}},\theta_S-\pi^0_{W_S}\theta_S)\\ &\quad + \left(T_{S,h}^{\{k\}}-T_{F,h}^{\{k\}},k_S(\mathbf{n}\cdot\nabla\theta_S)\right)_{\Gamma_I} + \left(\chi_h^{\{k\}},\pi_{W_F}\theta_F\right)_{\Gamma_I}.\end{aligned} \tag{15}$$

Next, we define $\pi_\partial\theta_S = \pi_{W_S}\theta_S - \pi^0_{W_S}\theta_S$ which is non-zero only near the interface due to the definition of $\pi^0_{W_S}\theta_S$. Substituting $\pi^0_{W_S}\theta_S = \pi_{W_S}\theta_S - \pi_\partial\theta_S$ gives

$$\left(Q_S,\theta_S-\pi^0_{W_S}\theta_S\right) - a_3(T_{S,h}^{\{k\}},\theta_S-\pi^0_{W_S}\theta_S) = \left(Q_S,\theta_S-\pi_{W_S}\theta_S\right) - a_3(T_{S,h}^{\{k\}},\theta_S-\pi_{W_S}\theta_S) - (Q_S,\pi_\partial\theta_S) + a_3(T_{S,h}^{\{k\}},\pi_\partial\theta_S).$$

Finally, we define $\sigma^{\{k\}}$ such that

$$-\left(\sigma^{\{k\}},\pi_\partial\theta_S\right)_{\Gamma_I} = (Q_S,\pi_\partial\theta_S) - a_3(T_{S,h}^{\{k\}},\pi_\partial\theta_S). \tag{16}$$

Defining the quantity $\sigma^{\{k\}}$ above enables us to write the full error representation in the form presented in Theorem 5.1 below, in which each of the sources of error are clearly identified. In Section 6, we will see that the definition of $\sigma^{\{k\}}$ coincides with an existing flux recovery procedure.

Theorem 5.1. *The errors* $\mathbf{e}_u = \mathbf{u} - \mathbf{u}_h^{\{k\}}$, $e_p = p - p_h^{\{k\}}$, $e_{T_F} = T_F - T_{F,h}^{\{k\}}$ *and* $e_{T_S} = T_S - T_{S,h}^{\{k\}}$ *satisfy*

$$\begin{aligned}(\psi,\mathbf{e}) &= (\mathbf{f},\phi-\pi_V\phi) - a_1(\mathbf{u}_h^{\{k\}},\phi-\pi_V\phi) - c_1(\mathbf{u}_h^{\{k\}},\mathbf{u}_h^{\{k\}},\phi-\pi_V\phi) - b(\phi-\pi_V\phi,p_h) - d(T_{F,h}^{\{k\}},\phi-\pi_V\phi) - b(\mathbf{u}_h^{\{k\}},z\\ &\quad - \pi_Z z) + \left(Q_F,\theta_F-\pi_{W_F}\theta_F\right) - a_2(T_{F,h}^{\{k\}},\theta_F-\pi_{W_F}\theta_F) - c_2(\mathbf{u}_h^{\{k\}},T_{F,h}^{\{k\}},\theta_F-\pi_{W_F}\theta_F) + \left(Q_S,\theta_S-\pi_{W_S}\theta_S\right)\\ &\quad - a_3(T_{S,h}^{\{k\}},\theta_S-\pi_{W_S}\theta_S) + \left(T_{S,h}^{\{k\}}-T_{F,h}^{\{k\}},k_S(\mathbf{n}\cdot\nabla\theta_S)\right)_{\Gamma_I} + \left(\chi_h^{\{k\}},\pi_{W_F}\theta_F\right)_{\Gamma_I} - \left(\sigma^{\{k\}},\pi_{W_S}\theta_S\right)_{\Gamma_I}.\end{aligned} \tag{17}$$

The error comprises four components arising due to discretization errors in the momentum, continuity and energy equations in the fluid and solid, iterative component, and a component reflecting the error arising from the transfer of derivative information. Specifically, they are as follows.

(1) The discretization error in the momentum equations is

$$(\mathbf{f},\phi-\pi_V\phi) - a_1(\mathbf{u}_h^{\{k\}},\phi-\pi_V\phi) - c_1(\mathbf{u}_h^{\{k\}},\mathbf{u}_h^{\{k\}},\phi-\pi_V\phi) - b(\phi-\pi_V\phi,p_h) - d(T_{F,h}^{\{k\}},\phi-\pi_V\phi).$$

(2) The discretization error in the continuity equation is

$$-b(\mathbf{u}_h^{\{k\}},z-\pi_Z z).$$

(3) The discretization error in the energy equation in the fluid is

$$(Q_F,\theta_F-\pi_{W_F}\theta_F) - a_2(T_{F,h}^{\{k\}},\theta_F-\pi_{W_F}\theta_F) - c_2(\mathbf{u}_h^{\{k\}},T_{F,h}^{\{k\}},\theta_F-\pi_{W_F}\theta_F).$$

(4) The discretization error in the energy equation in the solid is

$$(Q_S,\theta_S-\pi_{W_S}\theta_S) - a_3(T_{S,h}^{\{k\}},\theta_S-\pi_{W_S}\theta_S).$$

(5) The iteration error is

$$(T_{S,h}^{\{k\}}-T_{F,h}^{\{k\}},k_S(\mathbf{n}\cdot\nabla\theta_S))_{\Gamma_I}.$$

(6) The transfer error is

$$(\chi_h^{\{k\}},\pi_{W_F}\theta_F)_{\Gamma_I} - (\sigma^{\{k\}},\pi_{W_S}\theta_S)_{\Gamma_I}.$$

Each of these error components may be estimated independently. The iteration error can be further decomposed as

$$\left(T_{S,h}^{\{k\}}-T_{F,h}^{\{k\}},k_S(\mathbf{n}\cdot\nabla\theta_S)\right)_{\Gamma_I} = \left(T_{S,h}^{\{k\}}-\pi_S T_{F,h}^{\{k\}},k_S(\mathbf{n}\cdot\nabla\theta_S)\right)_{\Gamma_I} + \left(\pi_S T_{F,h}^{\{k\}}-T_{F,h}^{\{k\}},k_S(\mathbf{n}\cdot\nabla\theta_S)\right)_{\Gamma_I},$$

which represents an iteration error and a projection error. Obviously the choice of derivative information, $\chi_h^{\{k\}}$ that is transferred from Ω_S to Ω_F has a significant impact on the transfer error. We return to this issue in Section 6.

5.4. Adaptive refinement

We employ the standard "optimization framework" based on the Principle of Equidistribution to guide adaptive mesh refinement [16,17,3,2]. This approach is based on a error bound written as a sum of positive element contributions. A calculus of variations argument shows that the optimal mesh is obtained when the element contributions are equal, leading to the strategy of refining some fraction of elements with the largest element contributions at each refinement stage. In practice, we compute an element tolerance by taking the global tolerance and dividing by the number of elements, then refine some fraction of those elements whose element contribution is larger than the local tolerance.

We obtain the required error bound from the *a posteriori* error representation (17) by writing each term in the representation as a sum of integrals over the elements and then inserting norms. This removes cancelation of errors between elements, which is required for the standard argument about obtaining an optimal mesh. The local error indicator on an element $K \in \mathcal{T}_F$ is

$$\begin{aligned}\eta_{K,S} = \Big| &(\boldsymbol{f}, \phi - \pi_V\phi)_K - a_1(\boldsymbol{u}_h^{\{k\}}, \phi - \pi_V\phi)_K - c_1(\boldsymbol{u}_h^{\{k\}}, \boldsymbol{u}_h^{\{k\}}, \phi - \pi_V\phi)_K - b(\phi - \pi_V\phi, p_h)_K - d(T_{F,h}^{\{k\}}, \phi - \pi_V\phi)_K \\ &- \left(\boldsymbol{u}_h^{\{k\}}, z - \pi_Z z\right)_K + (Q_F, \theta_F - \pi_{W_F}\theta_F)_K - a_2(T_{F,h}^{\{k\}}, \theta_F - \pi_{W_F}\theta_F)_K - c_2(\boldsymbol{u}_h^{\{k\}}, T_{F,h}^{\{k\}}, \theta_F - \pi_{W_F}\theta_F)_K\Big| \end{aligned} \tag{18}$$

and an indicator on $K \in \mathcal{T}_S$,

$$\eta_{K,S} = \left|(Q_S, \theta_S - \pi_{W_S}\theta_S)_K - a_3(T_{S,h}^{\{k\}}, \theta_S - \pi_{W_S}\theta_S)_K + \left(\chi_h^{\{k\}}, \pi_{W_S}\theta_S\right)_{\Gamma_I} - \left(\sigma^{\{k\}}, \pi_{W_S}\theta_S\right)_{\partial K \cap \Gamma_I}\right|, \tag{19}$$

with the obvious notation for localizing the forms to an element K.

Note that we dropped the projection error and the iteration error terms from the element contribution expression. The reason is that even if these expressions are large, it is not clear that refining the mesh will reduce these sources of error.

Note that the number of degrees of freedom in the discretization for the two components in the coupled Boussinesq system (1) are very different. The solid discretization contains only a temperature variable, while the fluid discretization contains a temperature variable as well as two (or three) velocity variables and a pressure variable. As a consequence, refining the fluid mesh requires a greater increase in the computational resources than refining the solid mesh. Consequently, we modify the standard approach to more efficiently balance the computational work between the physical components. Let TOL denote the global error tolerance, and let N_F and N_S be the number of degrees of freedom associated with the fluid mesh and the solid mesh, respectively. We allocate the global error to each component using

$$\mathrm{TOL}_F = \frac{N_F}{N_F + N_S}\mathrm{TOL} \quad \text{and} \quad \mathrm{TOL}_S = \frac{N_S}{N_F + N_S}\mathrm{TOL},$$

and refine each mesh based on these component tolerances. These allocations are dynamically modified for each iteration of the refinement algorithm.

6. Flux correction

The numerical example in Section 4 suggests that a straightforward operator decomposition can result in a loss of order of convergence. To mitigate this effect, we use a post-processing technique developed by Wheeler [33] and Carey [10,9] originally to recover boundary flux values for finite element solutions of elliptic problems.

We define the set of elements in $\mathcal{T}_{S,h}$ that intersect the boundary by

$$\mathcal{T}_{S,h}^{\Gamma_I} = \{K \in \mathcal{T}_{S,h} | \overline{K} \cap \Gamma_I \neq \emptyset\},$$

and the corresponding space

$$\Sigma_h = \left\{v \in P^2(K) \text{ with } K \in \mathcal{T}_{S,h}^{\Gamma_I},\ v(\eta_i) = 0 \text{ if } \eta_i \notin \Gamma_I\right\},$$

where $\{\eta_i\}$ denotes the nodes of element K, so the degrees of freedom correspond to the nodes on the boundary. We seek $\sigma^{\{k\}} \in \Sigma_h$ satisfying

$$-\left(\sigma^{\{k\}}, v\right)_{\Gamma_I} = (Q_S, v) - a_3(T_{S,h}^{\{k\}}, v), \quad \text{for all } v \in \Sigma_h, \tag{20}$$

where $T_{S,h}^{\{k\}}$ solves (7). This definition of $\sigma^{\{k\}}$ is equivalent to the earlier definition (16). Green's identity implies that $\sigma^{\{k\}}$ gives an approximation to the normal flux on the boundary which is relatively inexpensive to compute.

In Algorithm 2, we solve (7) and compute the recovered flux by post-processing the finite element solution, $T_{S,h}^{\{k\}}$. Next, we set $\chi^{\{k\}} = \sigma^{\{k\}}$ in the weak form of the energy equation in (8), i.e. we solve

$$a_2(T_{F,h}^{\{k\}}, w) + c_2(\boldsymbol{u}_h^{\{k\}}, T_{F,h}^{\{k\}}, w) = (Q_F, w) - (\sigma^{\{k\}}, w)_{\Gamma_I}. \tag{21}$$

Table 2
Mesh sizes, number of elements and L^2 errors for the motivational example using the recovered flux.

h	NELEM	Fluid temperature	Solid temperature	x-Velocity	y-Velocity	Pressure
1/2	120	3.55E−4	3.12E−4	1.74E−4	2.34E−4	2.55E−1
1/4	480	5.11E−5	5.22E−5	1.93E−5	2.82E−5	7.73E−2
1/8	1920	6.95E−6	6.65E−6	2.43E−6	3.57E−6	1.91E−2
Conv. Rates		2.84	2.78	3.08	3.02	1.87

In general, the accuracy of the recovered boundary flux approximation depends on the regularity of an associated Green's function [25,34]. However regardless of accuracy, post-processing the solution using the recovered boundary flux leads to a cancelation of the "transfer error" term in the *a posteriori* error representation formula for the post-processed solution, see Section 6.1. So in this situation, use of the recovered flux is motivated by a fortunate cancelation of errors and the accuracy of the recovered boundary flux is only of peripheral interest.

This flux recovery approach is closely related to the Steklov–Poincare projection [30] commonly used by nonoverlapping domain decomposition methods to compute the interface Schur complement operator [4,5,32]. The recovered flux is the natural approximation of the flux resulting from the condensation of the unknowns on the interface. The *a posteriori* analysis outlined in Appendix A suggests that an inaccurate approximation of the Steklov–Poincare operator results in a loss of order affecting all components of the multi-physics problem. We can prove this in the case of coupled elliptic problems [22].

6.1. Analysis of the transfer error

Recall that the transfer error is given by,

$$\left(\chi_h^{\{k\}}, \pi_{W_F}\theta_F\right)_{\Gamma_I} - \left(\sigma^{\{k\}}, \pi_{W_S}\theta_S\right)_{\Gamma_I}.$$

Clearly, the choice of $\chi_h^{\{k\}}$ affects this component of the error.

Suppose we set $\chi_h^{\{k\}} = k_S(\boldsymbol{n}\cdot\nabla T_{S,h}^{\{k\}})$, i.e. the finite element flux. Then

$$(\chi_h^{\{k\}}, \pi_{W_F}\theta_F)_{\Gamma_I} - (\sigma^{\{k\}}, \pi_{W_S}\theta_S)_{\Gamma_I} = \left(k_S(\boldsymbol{n}\cdot\nabla T_{S,h}^{\{k\}}) - \sigma^{\{k\}}, \pi_{W_F}\theta_F\right)_{\Gamma_I} + \left(\sigma^{\{k\}}, \pi_{W_F}\theta_F - \pi_{W_S}\theta_S\right)_{\Gamma_I},$$

which represents a transfer error and a projection error. If the transfer error is sufficiently large, it may dominate the estimate.

On the other hand, suppose we set $\chi_h^{\{k\}} = \sigma^{\{k\}}$, i.e. the recovered flux. Then

$$\left(\chi_h^{\{k\}}, \pi_{W_F}\theta_F\right)_{\Gamma_I} - \left(\sigma^{\{k\}}, \pi_{W_S}\theta_S\right)_{\Gamma_I} = \left(\sigma^{\{k\}}, \pi_{W_F}\theta_F - \pi_{W_S}\theta_S\right)_{\Gamma_I},$$

which represents only a projection error with *no transfer error*.

6.2. Motivational problem revisited

We reconsider the steady flow of a Newtonian fluid in a rectangular domain that is connected along one boundary to a solid that is heated from below as shown in Fig. 3. Now, we compute and pass the recovered boundary flux rather than the finite element flux, i.e. we set $\chi^{\{k\}} = \sigma^{\{k\}}$ in (8). We also compute a reference solution with a higher order method for comparison. In Table 2 we compare the L^2 errors in the velocity, pressure and temperature fields on a series of uniform meshes that align along the interface. Using the recovered boundary flux restores the optimal cubic order of convergence for each velocity and temperature component.

In [22], a similar *a posteriori* error analysis is applied to an operator decomposition approach for a system of elliptic equations coupled through an interface. We proved that the loss of convergence in the L^2 norm is due to the transfer of the finite element flux and can corrected by passing the recovered flux. Further, the effect of the recovered flux is accurately reflected in the *a posteriori* error estimates. Error estimates that are insensitive to this effect result in over-refinement.

In this paper, we use the Taylor–Hood finite element spaces, which require additional regularity, namely $\boldsymbol{u}\in H^3(\Omega_F),\ p\in H^2(\Omega_F),\ T_F\in H^3(\Omega_F)$, and $T_S\in H^3(\Omega_S)$, to prove optimal rates of convergence in the L^2 norm. Sufficient regularity can be shown for the Boussinesq approximation in $\mathbb{R}^2$ under certain assumptions on the data and the domain [7,13,27,14]. To our knowledge, these results are not known for the coupled system (1) in general domains. In Appendix A, we outline the mathematical analysis required to prove optimal rates of convergence in the case of sufficient regularity.

7. Numerical results

We now consider the flow past a cylinder as shown in Fig. 1. We solve the steady non-dimensionalized Boussinesq equations in the fluid domain,

$$\begin{cases} Re(\boldsymbol{u}^\star \cdot \nabla)\boldsymbol{u}^\star = -\nabla p^\star + \Delta \boldsymbol{u}^\star - \left(\frac{Pe}{PrFr} - \frac{Ra}{Pe} T_F^\star\right)\mathbf{j}, \\ -\nabla \cdot \boldsymbol{u}^\star = 0, \\ \boldsymbol{u}^\star \cdot \nabla T_F^\star = \frac{1}{Pe}\Delta T_F^\star + Q_F^\star, \end{cases}$$

and the non-dimensional heat equation in the solid domain,

$$\left\{ \frac{k_r}{Pe}\Delta T_S^\star = Q_S^\star, \right.$$

coupled by the interface conditions,

$$\begin{cases} T_S^\star = T_F^\star, \\ k_r(\boldsymbol{n} \cdot \nabla T_S^\star) = \boldsymbol{n} \cdot \nabla T_F^\star, \end{cases}$$

where $\star$ indicates dimensionless quantities and $\mathbf{j}$ is the unit vector in the cross-channel direction. The non-dimensional groups based on length scale L, velocity scale $\bar{U}$ and a temperature non-dimensionalization $T^\star = (T - T_0)/\Delta T$ are

$$Re = \frac{\bar{U}L}{\nu}, \quad Pe = \frac{\bar{U}L}{\kappa}, \quad Pr = \frac{\nu}{\kappa}, \quad Fr = \frac{\bar{U}^2}{gL}, \quad Ra = \frac{g\alpha L^3 \Delta T}{\nu\kappa}, \quad k_r = \frac{k_S}{k_F},$$

where $\boldsymbol{n}$ points from the fluid into the solid and $\kappa = k_F/(\rho c_p)$. We set T_0 to be the temperature of the fluid at the inlet and ΔT to be 1 K. Defining the velocity scale, $\bar{U}$, to be

$$\bar{U} = \frac{1}{L}\int_{-L/2}^{L/2} u(\hat{x}, y)dy,$$

for any $-3 \leqslant \hat{x} \leqslant 5$, and for a blockage ratio, $B = d/L = 0.5$, the computational study by Chen et al. [15] indicates that in the absence of buoyancy effects, the critical Reynolds number at which the steady symmetric flow becomes unstable at a Hopf bifurcation point exceeds 100.

To model the flow of water past a heated cylinder made from aluminium alloy, we set

$$Pr = 6.7833, \quad Pe = 5.0875 \times 10^2, \quad Fr = 4.5918 \times 10^{-3}, \quad k_r = 200.$$

The Reynolds number, as determined by the average inflow velocity, is 75. The fluid enters the domain with a non-dimensional temperature of 0, and we apply adiabatic boundary conditions on the top, bottom, and outflow boundaries. The solid cylinder has a hole in center which is maintained at a constant temperature one degree above the inflow temperature, giving a Rayleigh number of $Ra = 2.8336 \times 10^4$.

To estimate the average temperature in a region one channel diameter behind the center of the cylinder, we define

$$\psi_{T_F} = \frac{10}{\pi}\exp(-10(x-1)^2 - 10y^2).$$

We use the error indicators given by (18) and (19) to adaptively refine the discretizations in order to reduce the error in the average temperature of the solid to 0.1%.

In Table 3 we give the number of degrees of freedom, the dynamic component tolerance, the estimated linear functional, the estimated error, and the effectivity ratio for each iteration of the iterative scheme. The effectivity ratio is the estimated error divided by the true error, where the true error is approximated using a higher order approximation on a finer mesh. The individual components of the total error are provided in Table 4. The iterative component of the error is negligible since the Operator Decomposition Finite Element Method (Algorithm 2) is iterated until convergence at each step of the refinement algorithm.

We observe that the transfer component of the error dominates the total error. Note that the error can be negative since we are estimating the error in a linear functional. The component tolerance is initially much higher for the fluid mesh since

Table 3
Number of degrees of freedom, component error tolerance, estimated average temperature in the solid, estimated error, and effectivity ratio for the non-dimensional flow past a heated cylinder using the finite element flux.

Iteration	N_F	N_S	TOL_F	TOL_S	Est. Fctl.	Estimated error	Effectivity
1	5609	658	8.67E−4	1.33E−4	0.1270	1.14E−2	1.04
2	6541	840	8.86E−4	1.14E−4	0.1349	3.29E−3	1.05
3	19921	957	9.54E−4	4.58E−5	0.1283	9.72E−3	0.99
4	19921	1135	9.46E−4	5.39E−5	0.1367	1.37E−3	1.04
5	19921	1446	9.32E−4	6.77E−5	0.1370	1.07E−3	1.02
6	19921	1591	9.26E−4	7.40E−5	0.1372	8.96E−4	1.02
7	19921	1737	9.20E−4	8.02E−5	0.1380	1.09E−4	1.02
8	19921	2391	8.93E−4	1.07E−4	0.1381	1.18E−5	0.96

Table 4
Errors for the non-dimensional flow past a heated cylinder using the finite element flux.

Iteration	Fluid discretization	Solid discretization	Transfer	Projection	Total
1	6.09E−3	−6.39E−5	5.42E−3	−7.55E−6	1.14E−2
2	1.27E−4	−1.63E−5	3.22E−3	−4.64E−5	3.29E−3
3	−4.37E−5	−1.38E−5	9.87E−3	−9.63E−5	9.72E−3
4	−4.57E−5	−3.70E−6	1.51E−3	−9.01E−5	1.37E−3
5	−4.38E−5	−2.23E−6	1.16E−3	−4.26E−5	1.07E−3
6	−4.47E−5	−2.68E−6	9.47E−4	−4.09E−5	8.96E−4
7	−4.57E−5	−1.15E−6	1.59E−4	−2.83E−6	1.09E−4
8	−4.58E−5	9.43E−7	6.16E−5	−3.14E−6	1.18E−5

more degrees of freedom are associated with the fluid. As the solid mesh is refined, the number of degrees of freedom in the solid increases and the component tolerances become much closer.

For comparison, in Table 5 we provide the number of degrees of freedom, the dynamic component tolerance, the estimated linear functional, the estimated error, and the effectivity ratio when the recovered flux is passed. The individual components of the total error are provided in Table 6. We note that the transfer error has been greatly reduced, and the number of refinement iterations has also been reduced. Upon further inspection, we see that this is due to a fortuitous cancelation of the discretization and projection errors in the second iteration, eliminating the need for further adaptive refinements. This cancelation is the reason why only approximately one-third of the number of elements are required in the fluid domain as compared to the previous computation.

The final adaptive fluid mesh when using the finite element flux is given in Fig. 5. The adaptive scheme concentrates mesh refinement around the cylinder, in the recirculation zone, and directly upstream of the cylinder. The solution further downstream of the cylinder can be computed with less accuracy, as is shown by the coarser mesh. This is reminiscent of previous adaptive results for flow past a cylinder in [3,2]. The difference here is that our approach takes into account the interaction and the transfer of errors between the solid and the fluid.

In Fig. 6(a), we show the mesh produced by the adaptive strategy within the solid when using the finite element flux. Adaptivity is concentrated at the boundary due to the transfer error. For comparison, we also give the "adaptive" mesh when the recovered boundary flux is used Fig. 6(b). No refinement is necessary in this case since the transfer error has been greatly

Table 5
Number of degrees of freedom, component error tolerance, estimated average temperature in the solid, estimated error and effectivity ratio for the non-dimensional flow past a heated cylinder using the recovered flux.

Iteration	N_F	N_S	TOL_F	TOL_S	Est. Fctl.	Estimated error	Effectivity
1	5609	658	8.67E−4	1.33E−4	0.1323	6.14E−3	1.06
2	6710	658	9.11E−4	8.93E−5	0.1381	−6.32E−5	1.33

Table 6
Errors for the non-dimensional flow past a heated cylinder using the recovered flux.

Iteration	Fluid discretization	Solid discretization	Transfer	Projection	Total
1	6.14E−3	−1.69E−6	0	3.03E−6	6.14E−2
2	1.13E−4	−1.35E−6	0	−1.75E−4	−6.32E−5

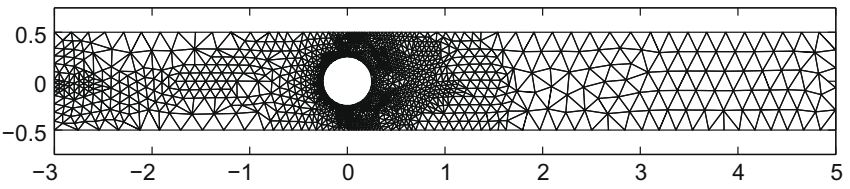

Fig. 5. Final adaptive mesh in the fluid.

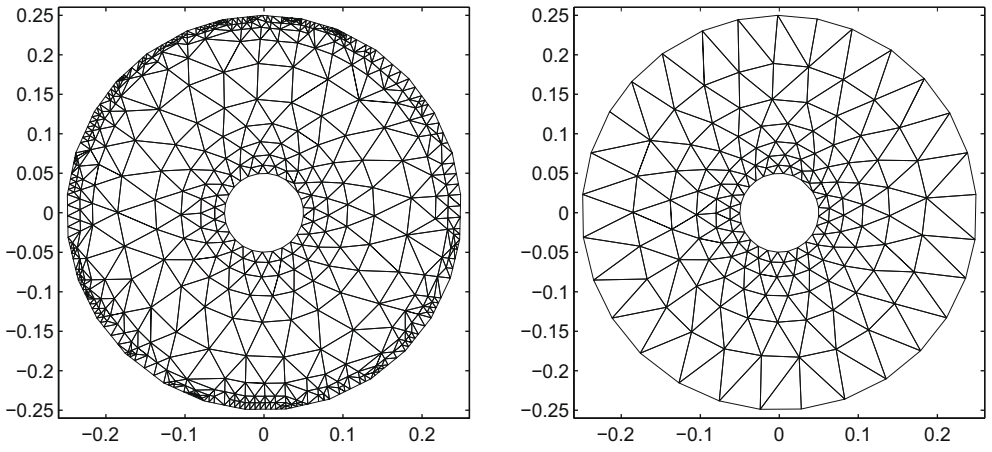

(a) Using FEM flux (b) Using recovered flux

Fig. 6. Final adaptive mesh in the solid: (a) when the finite element flux is passed and (b) when the recovered boundary flux is passed.

reduced. The refinement in the fluid mesh is qualitatively similar (even though it contains only one-third of the number of elements) and has been omitted for the sake of brevity.

8. Conclusion

We carry out an *a posteriori* error analysis of an multiscale operator decomposition finite element operator method for a multi-physics conjugate heat transfer problem. We adapt the *a posteriori* approach based on variational analysis, residuals and the generalized Green's function to derive accurate error estimates which are then used to guide adaptive mesh refinement. Modifications to the standard error analysis account for the transfer of error between components of the decomposed operator, interpolation error, and error arising from iterative solution. The analysis clearly identifies the lower order accuracy of the transferred gradient information as the reason for the loss of accuracy with respect to mesh size that is observed in the operator decomposition method. We adapt a boundary flux method to postprocess the solution and so recover the lost accuracy.

Acknowledgments

D. Estep's work is supported in part by the Department of Energy (DE-FG02-04ER25620, DE-FG02-05ER25699, DE-FC02-07ER54909), the National Aeronautics and Space Administration (NNG04GH63G), the National Science Foundation (DMS-0107832, DMS-0715135, DGE-0221595003, MSPA-CSE-0434354, ECCS-0700559), Idaho National Laboratory (00069249), and the Sandia Corporation (PO299784).

Appendix A. Optimal L^2 error bounds

Given an appropriate choice of data for the adjoint problem (12), the *a posteriori* error estimate (17) can be used to derive a bound on the L^2 error if the solution to (1) and (12) are sufficiently smooth. As discussed in Section 6.2, such regularity results exist only for a limited range of problems for the Boussinesq approximation [7,13,27,14]. Nevertheless, the error representation can be broken down into four terms, each containing one or more of the following errors: discretization, projection, iteration, and transfer. From this decomposition of the error representation, it is immediately clear that the transfer error will be the asymptotically dominant component if the solutions are sufficiently smooth.

Let $\boldsymbol{u}$, p, T_F and T_S solve (1), and $\boldsymbol{u}_h^{\{k\}}$, $p_h^{\{k\}}$, $T_{F,h}^{\{k\}}$ and $T_{S,h}^{\{k\}}$ be the finite element solutions from the operator decomposition method at the kth iteration. Let $\boldsymbol{\phi}$, z, θ_F and θ_S solve the adjoint problem (12) with $\boldsymbol{\psi}_{\boldsymbol{u}} = \mathbf{0}$, $\psi_p = 0$, $\psi_{T_F} = e_{T_F}/\|e_{T_F}\|_{\Omega_F}$ and $\psi_{T_S} = e_{T_S}/\|e_{T_S}\|_{\Omega_S}$. Starting with (17), integration by parts over each element K gives

$$\|e_{T_F}\|_{\Omega_F} + \|e_{T_S}\|_{\Omega_S} = I_1 + I_2 + I_3 + I_4,$$

where

$$I_1 = \sum_{K\in\tau_{F,h}} \left(R_1(\boldsymbol{u}_h^{\{k\}}, p_h^{\{k\}}, T_{F,h}^{\{k\}}), \boldsymbol{\phi} - \pi_V\boldsymbol{\phi}\right)_K + \frac{1}{2}\left(\left[\mu\frac{\partial \boldsymbol{u}_h^{\{k\}}}{\partial \boldsymbol{n}}\right], \boldsymbol{\phi} - \pi_V\boldsymbol{\phi}\right)_{\partial K} + \sum_{K\in\tau_{F,h}} \left(R_2(\boldsymbol{u}_h^{\{k\}}), z - \pi_Z z\right)_K$$
$$+ \sum_{K\in\tau_{F,h}} \left(R_3(\boldsymbol{u}_h^{\{k\}}, T_{F,h}^{\{k\}}), \theta_F - \pi_{W_F}\theta_F\right)_K + \frac{1}{2}\left([k_F(\boldsymbol{n}\cdot\nabla T_{F,h}^{\{k\}})], \theta_F - \pi_{W_F}\theta_F\right)_{\partial K} + \sum_{K\in\tau_{S,h}} \left(R_4(T_{S,h}^{\{k\}}), \theta_S - \pi_{W_S}\theta_S\right)_K$$
$$+ \frac{1}{2}\left([k_S(\boldsymbol{n}\cdot\nabla T_{S,h}^{\{k\}})], \theta_S - \pi_{W_S}\theta_S\right)_{\partial K},$$

$$I_2 = \left(k_F(\boldsymbol{n}\cdot\nabla T_{F,h}^{\{k\}}), \theta_F - \pi_{W_F}\theta_F\right)_{\Gamma_I} - \left(k_S(\boldsymbol{n}\cdot\nabla T_{S,h}^{\{k\}}), \theta_S - \pi_{W_S}\theta_S\right)_{\Gamma_I},$$
$$I_3 = \left(k_S(\boldsymbol{n}\cdot\nabla\theta_S), T_{S,h}^{\{k\}} - T_{F,h}^{\{k\}}\right)_{\Gamma_I},$$
$$I_4 = \left(\chi^{\{k\}}, \pi_{W_F}\theta_F\right)_{\Gamma_I} - \left(\sigma^{\{k\}}, \pi_{W_S}\theta_S\right)_{\Gamma_I},$$

with $[\cdot]$ denoting the jump across an element edge and

$$R_1\left(\boldsymbol{u}_h^{\{k\}}, p_h^{\{k\}}, T_{F,h}^{\{k\}}\right) = \boldsymbol{f} + \mu\Delta\boldsymbol{u}_h^{\{k\}} - \rho_0(\boldsymbol{u}_h^{\{k\}}\cdot\nabla)\boldsymbol{u}_h^{\{k\}} - \nabla p_h^{\{k\}} - \rho_0\beta T_{F,h}^{\{k\}}\mathbf{g},$$
$$R_2(\boldsymbol{u}_h^{\{k\}}) = \nabla\cdot\boldsymbol{u}_h^{\{k\}},$$
$$R_3(\boldsymbol{u}_h^{\{k\}}, T_{F,h}^{\{k\}}) = Q_F + k_F\Delta T_{F,h}^{\{k\}} - \rho_0 c_p(\boldsymbol{u}_h^{\{k\}}\cdot\nabla T_{F,h}^{\{k\}}),$$
$$R_4(T_{S,h}^{\{k\}}) = Q_S + k_S\Delta T_{S,h}^{\{k\}}.$$

The first term, I_1, is the standard *a posteriori* weighted residual at the kth iteration. This term does not contain any transfer or, iteration error, and therefore is not affected by non-matching triangulations along the interface. If the solution to (1) and the adjoint solutions are sufficiently smooth, then standard techniques (see e.g. [16,17,22]) can be used to show the optimal rate of convergence for I_1 if the mesh is quasi-uniform.

The second term, I_2, represents the jump term along the interface arising after integration by parts on the elements adjacent to the interface. We split this term into three components,

$$I_2 = \left(\chi^{\{k\}}, \pi_{W_S}\theta_S - \pi_{W_F}\theta_F\right)_{\Gamma_I} + \left(k_F(\boldsymbol{n}\cdot\nabla T_{F,h}^{\{k\}}) - \chi^{\{k\}}, \theta_F - \pi_{W_F}\theta_F\right)_{\Gamma_I} + \left(\chi^{\{k\}} - k_S(\boldsymbol{n}\cdot\nabla T_{S,h}^{\{k\}}), \theta_S - \pi_{W_S}\theta_S\right)_{\Gamma_I}.$$

The first component is a projection error which is zero if the triangulations match along the interface. Otherwise, if the solution to (1) and the adjoint solutions are sufficiently smooth, then the projection error can be bounded using standard techniques, although the convergence rate will be slightly slower as compared with the previous terms as is expected for non-matching interface triangulations [22,30]. The second and third components can be bounded using the same regularity assumptions and techniques as for the jump terms in I_1 and will converge at the same rate.

The third term, I_3, represents the discontinuity in the temperature field along the interface. We split this term into two components,

$$I_3 = \left(k_S(\boldsymbol{n}\cdot\nabla\theta_S), T_{S,h}^{\{k\}} - \pi_{W_S}T_{F,h}^{\{k\}}\right)_{\Gamma_I} + \left(k_S(\boldsymbol{n}\cdot\nabla\theta_S), \pi_{W_S}T_{F,h}^{\{k\}} - T_{F,h}^{\{k\}}\right)_{\Gamma_I}.$$

The first component is an iterative error and can be driven to zero by increasing the number of iterations. The second component is a projection error which is either zero (in the case of matching triangulations), or can be bounded using the same regularity assumptions and techniques as above with a slightly suboptimal rate of convergence.

Finally, the fourth term, I_4, represents the difference between the numerical flux passed from Ω_S to Ω_F and the flux obtained via the boundary-flux correction technique. We split this term into two components,

$$I_4 = \left(\chi^{\{k\}} - \sigma^{\{k\}}, \pi_{W_F}\theta_F\right)_{\Gamma_I} + \left(\sigma^{\{k\}}, \pi_{W_F}\theta_F - \pi_{W_S}\theta_F\right)_{\Gamma_I}.$$

The first component will be zero if the flux from the boundary-flux correction technique is transferred. If the finite element flux is transferred, then convergence rate for I_4 will be dominated by the error in the finite element flux, which typically converges one order lower than the previous terms. The second component is a projection error and can be treated similar to the other projection errors with the same suboptimal rate of convergence.

References

[1] R.A. Adams, Sobolev Spaces, Academic Press, 1975.
[2] W. Bangerth, R. Rannacher, Adaptive Finite Element Methods for Differential Equations, Birkhauser Verlag, 2003.
[3] R. Becker, R. Rannacher, An optimal control approach to a posteriori error estimation in finite element methods, Acta Numer. (2001) 1–102.
[4] P.E. Bjorstad, O.B. Widlund, Iterative methods for the solution of elliptic problems on regions partitioned into substructures, SIAM J. Numer. Anal. 23 (1986) 1097–1120.
[5] J.H. Bramble, J.E. Pasciak, A.H. Schatz, The construction of preconditioners for elliptic problems by substructuring. I, Math. Comput. 47 (1986) 103–134.

[6] S.C. Brenner, L.R. Scott, The Mathematical Theory of Finite Element Methods, Springer, 2002.
[7] J.R. Cannon, E. Dibenedetto, The initial value problem for the Boussinesq equations with data in L super p, in: Approximation Methods for Navier–Stokes Problems, Proceedings of the Symposium, Paderborn, West Germany, September 9–15, 1979. (A81-36526 16-34), Springer-Verlag, Berlin, 1980, pp. 129–144.
[8] T. Cao, D. Kelly, M. Ainsworth, Some useful techniques for pointwise and local error estimates of the quantities of interest in the finite element approximation, ANZIAM 42 (2000) 317–339.
[9] G.F. Carey, Derivative calculation from finite element solutions, Comput. Methods Appl. Mech. Eng. 35 (1982) 1–14.
[10] G.F. Carey, S.S. Chow, M.K. Seager, Approximate boundary-flux calculations, Comput. Methods Appl. Mech. Eng. 50 (1985) 107–120.
[11] V. Carey, D. Estep, S. Tavener, A posteriori analysis and adaptive error control for multiscale operator decomposition solution of elliptic systems I: Triangular systems, SIAM J. Numer. Anal. (2009) 740–761.
[12] V. Carey, D. Estep, S. Tavener, A posteriori analysis and adaptive error control for operator decomposition methods for elliptic systems II: Fully coupled systems, in preparation.
[13] D. Chae, O.Y. Imanuvilov, Generic solvability of the axisymmetric 3-D Euler equations and the 2-D Boussinesq equations, J. Differ. Equat. 156 (1999) 1–17.
[14] D. Chae, S.-K. Kim, H.-S. Nam, Local existence and blow-up criterion of Hölder continuous solutions of the Boussinesq equations, Nagoya Math. J. 155 (1999) 55–80.
[15] J.-H. Chen, W. Pritchard, S. Tavener, Bifurcation for flow past a cylinder between parallel planes, J. Fluid Mech. 284 (1995) 23–41.
[16] K. Eriksson, D. Estep, P. Hansbo, C. Johnson, Introduction to adaptive methods for differential equations, Acta Numer. (1995) 105–158.
[17] K. Eriksson, D. Estep, P. Hansbo, C. Johnson, Computational Differential Equations, Cambridge University Press, Cambridge, 1996.
[18] D. Estep, A posteriori error bounds and global error control for approximations of ordinary differential equations, SIAM J. Numer. Anal. 32 (1995) 1–48.
[19] D. Estep, V. Ginting, D. Ropp, J. Shadid, S. Tavener, An a posteriori – a priori analysis of multiscale operator splitting, SIAM J. Numer. Anal. 46 (2008) 1116–1146.
[20] D. Estep, M. Holst, M. Larson, Generalized Green's functions and the effective domain of influence, SIAM J. Sci. Comput. 26 (2004) 1314–1339.
[21] T. Wildey, A posteriori analysis of operator decomposition for interface problems, Ph.D. Thesis, Department of Mathematics, Colorado State University, 2007.
[22] D. Estep, S. Tavener, T. Wildey, A posteriori analysis and improved accuracy for an operator decomposition solution of a conjugate heat transfer problem, SIAM J. Numer. Anal. 46 (2008) 2068–2089.
[23] D. Estep, R. Williams, M. Larson, Estimating the error of numerical solutions of systems of reaction–diffusion equations, Mem. Am. Math. Soc. 146 (2000).
[24] M. Giles, Stability analysis of numerical interface boundary conditions in fluid–structure thermal analysis, Int. J. Numer. Methods Fluids 25 (1997) 421–436.
[25] M. Giles, M.G. Larson, J.M. Levenstam, E. Suli, Adaptive error control for finite element approximations of the lift and drag coefficients in viscous flow, Tech. Report NA-97-06, Oxford University Computing Laboratory, 1997.
[26] V. Heuveline, R. Rannacher, Duality-based adaptivity in the hp-finite element method, J. Numer. Math. 11 (2003) 1–18.
[27] T. Hou, C. Li, Global well-posedness of the viscous Boussinesq equations, Discrete Contin. Dynam. Syst. 12 (2005) 1–12.
[28] M.G. Larson, F. Bengzon, Adaptive finite element approximation of multiphysics problems, Commun. Numer. Methods Eng. 24 (2008) 505–521.
[29] M.G. Larson, R. Soderlund, F. Bengzon, Adaptive finite element approximation of coupled flow and transport problems with applications in heat transfer, Int. J. Numer. Methods Fluids 9 (2008) 1397–1420.
[30] A. Quarteroni, A. Valli, Domain Decomposition Methods for Partial Differential Equations, Oxford University Press, UK, 2005.
[31] J. Rice, P. Tsompanopoulus, E. Vavalis, Interface relaxation methods for elliptic differential equations, Appl. Numer. Math. 32 (2000) 219–245.
[32] B. Smith, P. Bjorstad, W. Gropp, Domain Decomposition, Cambridge University Press, 1994.
[33] M. Wheeler, A Galerkin procedure for estimating the flux for two-point boundary-value problems using continuous piecewise-polynomial spaces, Numer. Math 2 (1974) 99–109.
[34] T. Wildey, D. Estep, S. Tavener, A posteriori error estimation of boundary flux, Commun. Numer. Methods Eng. 24 (2008) 421–434.
[35] D. Yang, A parallel nonoverlapping Schwarz domain decomposition method for elliptic interface problems, IMA J. Numer. Anal. 16 (1996) 75–91.
[36] I. Yotov, Interface solvers and preconditioners of domain decomposition type for multiphase flow in multiblock porous media, Adv. Comput.: Theory Pract. 7 (2001) 157–167.